A Linear Relationship between Vertical Velocity and Condensation Processes in Deep Convection

LEAH D. GRANT,[a] SUSAN C. VAN DEN HEEVER,[a] ZIAD S. HADDAD,[b] JENNIE BUKOWSKI,[a] PETER J. MARINESCU,[a,c]
RACHEL L. STORER,[b,d] DEREK J. POSSELT,[b] AND GRAEME L. STEPHENS[b]

[a] Department of Atmospheric Science, Colorado State University, Fort Collins, Colorado
[b] Jet Propulsion Laboratory, California Institute of Technology, Pasadena, California
[c] Cooperative Institute for Research in the Atmosphere, Fort Collins, Colorado
[d] Joint Institute for Regional Earth System Science and Engineering, University of California Los Angeles, Los Angeles, California

ABSTRACT: Vertical velocities and microphysical processes within deep convection are intricately linked, having wide-ranging impacts on water and mass vertical transport, severe weather, extreme precipitation, and the global circulation. The goal of this research is to investigate the functional form of the relationship between vertical velocity (w) and microphysical processes that convert water vapor into condensed water (M) in deep convection. We examine an ensemble of high-resolution simulations spanning a range of tropical and midlatitude environments, a variety of convective organizational modes, and different model platforms and microphysics schemes. The results demonstrate that the relationship between w and M is robustly linear, with the slope of the linear fit being primarily a function of temperature and secondarily a function of supersaturation. The R^2 of the linear fit is generally above 0.6 except near the freezing and homogeneous freezing levels. The linear fit is examined both as a function of local in-cloud temperature and environmental temperature. The results for in-cloud temperature are more consistent across the simulation suite, although environmental temperatures are more useful when considering potential observational applications. The linear relationship between w and M is substituted into the condensate tendency equation and rearranged to form a diagnostic equation for w. The performance of the diagnostic equation is tested in several simulations, and it is found to diagnose the storm-scale updraft speeds to within 1 m s^{-1} throughout the upper half of the clouds. Potential applications of the linear relationship between w and M and the diagnostic w equation are discussed.

KEYWORDS: Convective-scale processes; Deep convection; Updrafts/downdrafts; Vertical motion; Cloud microphysics; Cloud resolving models

---

1. Introduction

Convective clouds are an important source of freshwater to life on Earth. The characteristics and intensity of deep convection are fundamentally linked to the vertical motion within such cloud systems. Deep convective updrafts transport mass, water, energy, aerosol, and pollutants from the boundary layer to the mid- and upper troposphere and stratosphere (Cotton et al. 1995; Dauhut et al. 2015; Barth et al. 2015), and downdrafts carry air and its properties from the free troposphere to near the surface or from the lower stratosphere to the upper tropopause (Betts 1976; Zipser 1977; Pan et al. 2014). Deep convective cores were originally proposed to fuel the Hadley circulation and thus play an essential role in the global circulation (Riehl and Malkus 1958), and ongoing research has advanced and refined this understanding (Zipser 2003; Fierro et al. 2009, 2012; McGee and van den Heever 2014). The strength and width of deep convective updrafts in severe convection, such as supercells, plays a role in hail formation, especially large hail (Browning and Foote 1976; Nelson 1983; Grant and van den Heever 2014; Dennis and Kumjian 2017; Kumjian and Lombardo 2020), and the longevity of convective updrafts is an essential ingredient of storm-accumulated precipitation (Doswell et al. 1996; Marinescu

et al. 2016; Nielsen and Schumacher 2018). It is therefore of utmost importance to gain a better understanding of vertical motions within deep convection to better characterize their impacts on weather and climate.

The relation between vertical motion and cloud microphysical properties has long been appreciated. Politovich and Cooper (1988), for example, found a linear relation between w and supersaturation based on aircraft observations of mostly liquid clouds over Montana. Earlier studies (e.g., Squires 1952) also call out similar relations in warm clouds. Our investigation, however, expands beyond these previous studies, exploring in detail this relation for a more complex range of processes associated with deep convection. The overarching goal of this study is to address the question, *what is the specific functional form of the relationship between vertical velocity (w) and microphysical process rates that convert water vapor into condensed water (M) in deep convection*? We first discuss why we expect a relationship between w and M and what factors may affect it. van den Heever et al. (2018) and Stephens et al. (2020) examined several simulations of deep convection using a single numerical model and proposed that a linear relationship exists between w and M in deep convection, but they did not explore the underlying physical processes. In this study, we fully explore the nature of this relation using an extensive suite of high-resolution cloud-resolving model simulations. A subset of the suite was

---

Corresponding author: Leah D. Grant, leah.grant@colostate.edu

examined in van den Heever et al. (2018) and Stephens et al. (2020), but here we include different types of convection evolving in varying environments and multiple modeling platforms and microphysics schemes. We also discuss physical processes explaining where the linear relationship works in deep convection and why, and therefore the theoretical underpinning of the results in van den Heever et al. (2018) and Stephens et al. (2020). Finally, we describe the implications of the results for future observational platforms.

2. Background

One of the main factors that shape microphysical processes in clouds is the degree to which a cloudy parcel is supersaturated. Adiabatic cooling in updrafts leads to decreases in the saturation water vapor mixing ratio and hence increases in relative humidity. Eventually this rising motion produces supersaturation, which is the primary driver for cloud droplet nucleation, condensation of water vapor onto liquid water droplets, and deposition of water vapor onto ice particles. This relationship is revealed in the condensation equation for a population of cloud droplets [e.g., Rogers and Yau 1989; Korolev and Mazin 2003, their Eq. (4)]:

$$C = \frac{n_c}{\rho} 4\pi r \rho_l G(T,P)(S-1), \qquad (1)$$

where C is the rate of condensation onto the population of cloud droplets (kg kg^{-1} s^{-1}), n_c is the cloud droplet number concentration (m^{-3}), ρ is the air density, r is the cloud droplet radius, ρ_l is the density of liquid water, T is the temperature, P is the pressure, and S is the saturation ratio such that $(S-1)$ is the fractional supersaturation. $4\pi r \rho_l G(T,P)(S-1)$ is the condensation rate onto a single cloud droplet with radius r where $G(T,P)$ (m^2 s^{-1}) modulates the condensation rate based on the temperature and pressure [see, e.g., Rogers and Yau (1989) for the full form]. Here, a monodisperse cloud droplet population has been assumed. The primary point to be taken from Eq. (1) is that supersaturation is the driver of condensation, and the condensation process is modulated by pressure, temperature, air density, droplet radius, and droplet concentration.

Supersaturation is generated by cooling within updrafts, which can be seen from a simple equation for the rate of change of saturation ratio [Rogers and Yau 1989; see also Squires (1952), or Korolev and Mazin (2003), which includes ice processes]:

$$\frac{dS}{dt} = w \frac{\partial r_{vs}}{\partial z} - C, \qquad (2)$$

where w is the vertical velocity, r_{vs} is the saturation water vapor mixing ratio, and C is given by Eq. (1). Equation (2) shows that generation of supersaturation is dependent on the updraft vertical velocity and the rate of condensation, where the former is a source of supersaturation and the latter is a supersaturation sink. The updraft vertical velocity is scaled by the vertical gradient in saturation water vapor mixing ratio and therefore by temperature and pressure. When evaluating Eqs. (1) and (2), it is often assumed that w is a constant value or follows a prescribed functional form (e.g., Politovich and

Cooper 1988; Feingold and Heymsfield 1992; Korolev and Mazin 2003; Reutter et al. 2009; Pinsky et al. 2013; Wang and Chen 2019). Earlier studies have also examined the relationship between Eqs. (1) and (2) and found that supersaturation reaches a quasi-equilibrium value such that w and supersaturation are linearly related (Squires 1952; Paluch and Knight 1984; Politovich and Cooper 1988; Korolev and Mazin 2003). However, these studies were mostly of liquid clouds and based on cloud droplets (and, in the case of Korolev and Mazin 2003, small ice crystals). Deep convection contains strong updrafts, a mixture of small and large liquid and ice hydrometeors whose temperatures can depart substantially from their surroundings, rapid vertical accelerations, and extreme turbulence. It is not clear that these simple relationships can be applied to deep convection.

Consider the tendency equations for the vertical velocity and condensed water mixing ratio (r_c) as they are programmed in a full physics numerical model (e.g., Cotton et al. 2010):

$$\underbrace{\frac{\partial w}{\partial t}}_{\substack{\text{Vertical} \\ \text{acceleration}}} = \underbrace{-\mathbf{V}\cdot\nabla w}_{\substack{\text{3D advection of} \\ \text{vertical velocity}}} \underbrace{-\frac{1}{\rho}\frac{\partial p}{\partial z}}_{\substack{\text{Vertical component} \\ \text{of pressure} \\ \text{gradient force}}} + \underbrace{g\left(\frac{\theta'}{\theta_0} + 0.61 r_v - r_c\right)}_{\substack{\text{Buoyancy: thermal,} \\ \text{water vapor, and} \\ \text{condensate loading}}} + \underbrace{D}_{\substack{\text{Subgrid} \\ \text{diffusion}}},$$

$$\qquad (3)$$

$$\underbrace{\frac{\partial r_c}{\partial t}}_{\substack{\text{Condensate mixing} \\ \text{ratio tendency}}} = \underbrace{-\mathbf{U}_h \cdot \nabla_h r_c}_{\substack{\text{Horizontal advection} \\ \text{of condensate}}} \underbrace{-[w - v_t]\frac{\partial r_c}{\partial z}}_{\substack{\text{Vertical advection} \\ \text{and hydrometeor} \\ \text{sedimentation}}} + \underbrace{M}_{\substack{\text{Microphysical} \\ \text{processes}}} + \underbrace{D}_{\text{Diffusion}}$$

$$\qquad (4)$$

where $\mathbf{V}$ is the three-dimensional wind vector, $\mathbf{U}_h$ is the horizontal component of the wind, ∇_h is the gradient operator in the horizontal direction, g is the acceleration due to gravity, θ' is the potential temperature perturbation from the model base-state potential temperature θ_0, r_v is the water vapor mixing ratio, D are subgrid diffusion tendencies, v_t is the condensate terminal velocity, and M represents all microphysical processes that convert water vapor into condensed water (i.e., M = condensation − evaporation + deposition − sublimation + nucleation of cloud water). Equations (3) and (4) are nonlinear coupled differential equations and are clearly more complex than Eqs. (1) and (2). w appears explicitly on the right-hand side of Eq. (4) in the vertical advection term, and w also influences M by generating supersaturation, as described by Eqs. (1) and (2). Furthermore, r_c appears explicitly on the right-hand side of Eq. (3) in the condensate loading term. Finally, M itself describes water phase changes that are associated with latent heating, and so M also directly influences buoyancy.

Given the various feedbacks that can be identified from Eqs. (3) and (4), strong updrafts, precipitating liquid and ice hydrometeors, and rapid accelerations, it is not obvious whether and how the simple relationships that can be obtained between w and M from Eqs. (1) and (2) can be applied to deep convection. However, van den Heever et al. (2018) and Stephens et al. (2020) suggested that the relationship between w and M is linear under some conditions based on simulation data. Here we fully explore this potential linear

TABLE 1. Summary of the ensemble of CRM simulations. All simulations using RAMS also use RAMS microphysics, whereas WRF simulations use Morrison microphysics as noted in the entry for "Numerical Model." The Supercell and Isolated Tropical WRF cases were configured to be as close as possible to the Supercell CTL RAMS and Isolated Tropical 250m RAMS cases, respectively. Vertical grid spacings with two numeric values separated by an arrow indicate surface and maximum grid spacings for stretched vertical grids.

| Simulation name	Type of convection	Numerical model	Simulation type	Horizontal, vertical grid spacings	Output interval	Reference
11 Aug Tropical Squall 17 Aug High-Shear Tropical 23 Feb Tropical Convection	Tropical oceanic squall line Sheared tropical oceanic cell Tropical continental convection	RAMS	Idealized	250 m, 50 → 450 m	30 s	Storer and Posselt (2019)
ACPC Scattered CLN ACPC Scattered POL	Scattered midlatitude continental cells, clean and polluted	RAMS	Case study	500 m, 50 → 300 m	1 min	Marinescu et al. (2021)
Isolated Tropical 250m Isolated Tropical 500m	Single-cell, tropical continental	RAMS	Idealized	250 m, 100 m 500 m, 200 m	1 min	Jensen et al. (2018)
Isolated Tropical WRF	Single-cell, tropical, continental	WRF (Morrison)	Idealized	250 m, 100 m	1 min	Setup based on Jensen et al. (2018)
MC3E Squall	Midlatitude squall line	RAMS	Case study	300 m, 75 → 300 m	1 min	Marinescu et al. (2017)
Multicells CTL Multicells H50 Multicells M25	Midlatitude multicells, various environmental humidity profiles	RAMS	Idealized	300 m, 25 → 300 m	1 min	Grant and van den Heever (2015)
Supercell CTL Supercell H50 Supercell M25	Midlatitude supercell, various environmental humidity profiles	RAMS	Idealized	300 m, 25 → 300 m	1 min	Grant and van den Heever (2014)
Supercell WRF	Midlatitude supercell	WRF (Morrison)	Idealized	300 m, 25 → 300 m	1 min	Setup based on Grant and van den Heever (2014)
Tropical Squall	Tropical oceanic squall line	RAMS	Idealized	250 m, 35 → 375 m	3 s	McGee and van den Heever (2014)
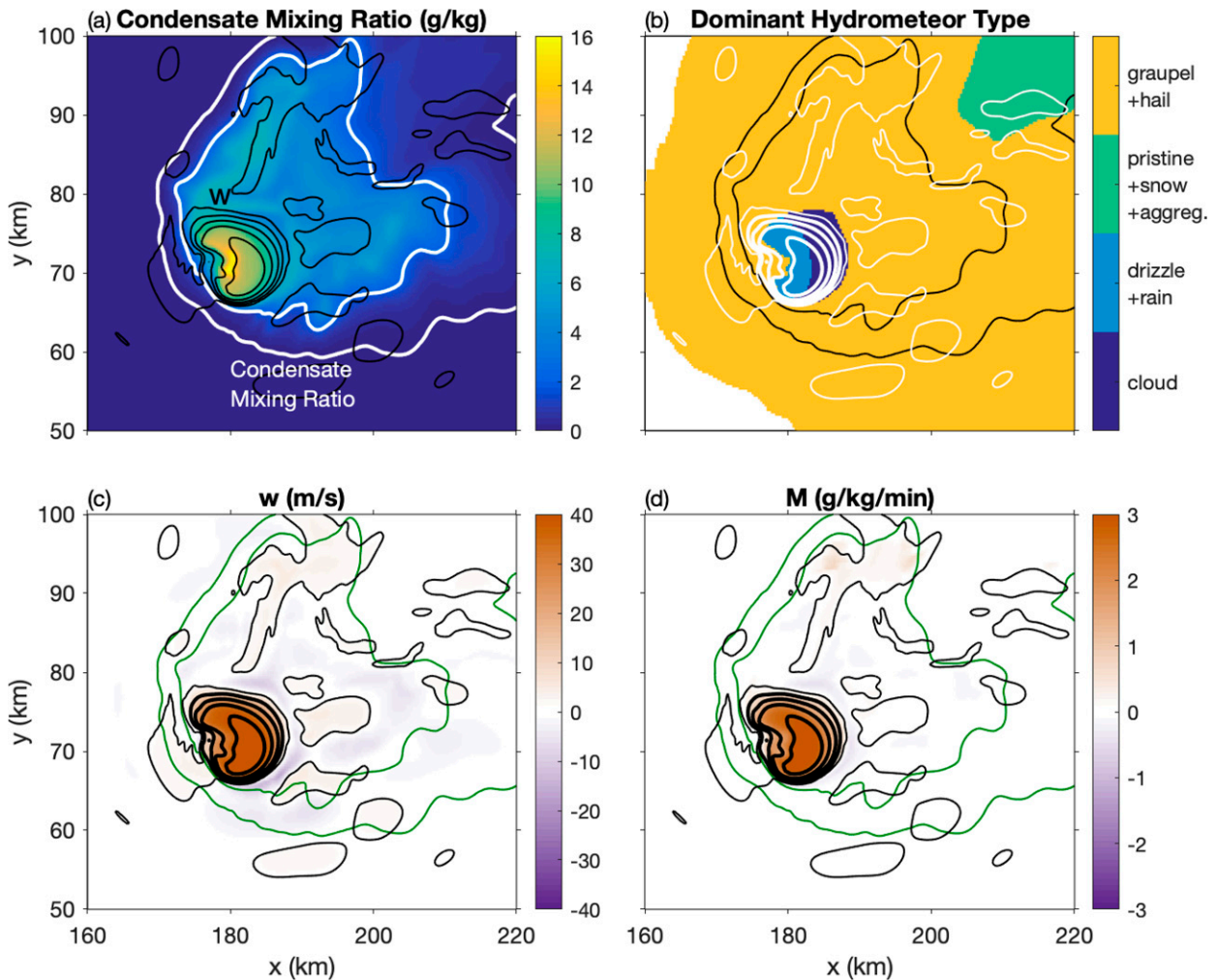
FIG. 1. Snapshots of (a) condensed water mixing ratio; (b) hydrometeor type with the largest mixing ratio in each grid box; (c) vertical velocity (w); and (d) the rate of conversion of all microphysical processes converting water vapor into condensed water (both liquid and ice) (M), accumulated over the output interval (1 min) for the Supercell CTL case. Results are shown at approximately 7 km AGL where the environmental (base state) temperature is $\sim-22.5°$C. Total condensate of 0.1 and 2 g kg^{-1} is outlined in white contours in (a), black contours in (b), and green contours in (c) and (d). Black contours in (a), (c), and (d) and white contours in (b) indicate w of 1 m s^{-1} (thin lines) and 10, 20, 30, and 40 m s^{-1} (thick lines).

relationship in a large ensemble of simulations, describe where it works and does not work well, and explore the associated physical processes.

3. Methodology

To address the goals of this study, we use an ensemble of cloud-resolving model (CRM) simulations of convection. Since the governing equations are not simplified in the CRMs included in the ensemble [see Eqs. (3) and (4)], full nonlinear interactions and feedbacks between the various terms are represented. High-resolution modeling simulations are therefore exceedingly useful tools with which to examine the relationships between the processes governing deep convective clouds.

The suite of CRM simulations is shown in Table 1 and represents a wide variety of storm types, lifetimes, and environments

[a subset of this suite was examined in van den Heever et al. (2018) and Stephens et al. (2020)]. First, the suite includes convective morphologies ranging from a single isolated convective tower and scattered unorganized convection to more organized multicell systems, squall lines, and supercells. Second, the ensemble includes both tropical and midlatitude atmospheric environments over maritime and continental regimes and in relatively clean and polluted aerosol conditions. Third, two different models and associated microphysics schemes are used. This CRM ensemble therefore allows us to determine whether the results of our analysis are robust across different types of convection, environments, and model platforms.

Most simulations are conducted using horizontal grid spacings between 250 and 300 m and therefore resolve the primary updraft circulations (Bryan et al. 2003; Lebo and Morrison 2015). The coarsest model output interval is one minute, with
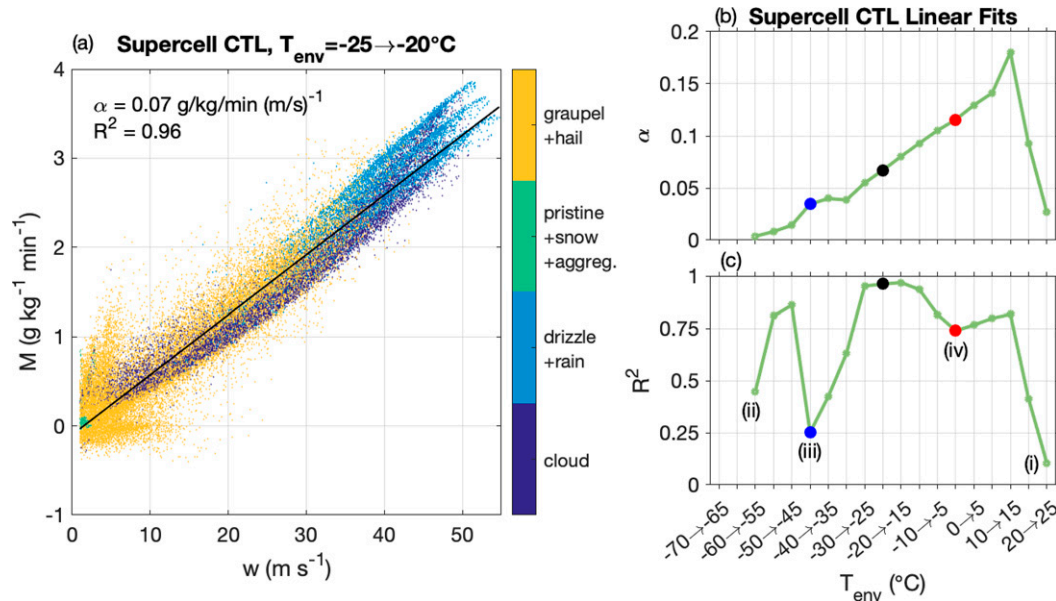
FIG. 2. (a) Scatterplot of w vs M for the Supercell CTL case. Results are shown for $w > 1$ m s^{-1} and environmental temperatures between $-25°$ and $-20°$C every 5 simulation minutes. Color shading indicates the hydrometeor type with the largest mixing ratio in each grid box at the end of the 1-min interval. Only every tenth grid point is plotted. The black line shows a linear regression fit; values of the slope of the linear fit (α) and R^2 are listed in the top left of the panel. (b) Slope of the linear fit and (c) R^2 of the linear fit for environmental temperatures every 5°C for the Supercell CTL case. Units in (b) are g kg^{-1} min^{-1} (m s^{-1})$^{-1}$. Black dots in (b) and (c) highlight the slope and R^2 for the fit shown in (a), while blue and red dots in (b) and (c) highlight the slope and R^2 for the fits shown in Figs. 3 and 4, respectively. Labeled points (i)–(iv) in (c) are discussed in the text. Note that (b) and (c) share the same x axis.

one simulation (Tropical Squall) having an output interval equal to the model time step (3 s). Finally, both idealized simulations and case study simulations of observed convective events are included. In total, the ensemble provides a rich dataset with which to explore potential relationships between vertical velocity and microphysical process rates.

To examine the relationship between vertical velocity and microphysical process rates in each of the ensemble simulations, we first look for all grid points where $w \geq 1$ m s^{-1}; this threshold has been used in prior studies to examine vertical velocities (e.g., Posselt et al. 2012; Park et al. 2020). At each grid point meeting the threshold, we average w at the current and previous output time and compare this time-averaged w to the value of M, the accumulated rate of conversion of water vapor to condensed water over the output time interval. In other words, M is accumulated over one simulation minute for the simulations with 1-min output intervals. M includes the net effects of condensation and evaporation between water vapor and preexisting liquid water, deposition and sublimation between water vapor and preexisting ice species, and nucleation of cloud water from the vapor phase that are output by the microphysics scheme. Note that a condensate threshold is *not* used in the analysis because we wanted to include as many points in the analysis as possible, and the same condensate threshold may not be appropriate at both warm and cold temperatures due to large changes in saturation mixing ratio with temperature. We tested the correlation analysis including a condensate threshold and found only minor differences in the results.

4. The relationship between w and M

a. Relationship between w and M for Supercell CTL example

Before we examine the relationship between w and M for the entire ensemble suite, we first look in detail at one example case, the Supercell CTL (Table 1). Figure 1 depicts plan views through an altitude in the mixed-phase region (environmental temperature $T_{env} = -22.5°$C), although the local in-cloud temperature (T_{local}) can vary from T_{env}; this is discussed in detail in section 4b. The updraft, which is primarily comprised of supercooled liquid water (Fig. 1b), contains high values of condensate (Fig. 1a), while the western-most edge of the updraft and the surrounding region is composed primarily of rimed ice (graupel and hail). Smaller ice crystals are found downstream in the anvil (Fig. 1b). Comparing the plan views of w (Fig. 1c) with M (Fig. 1d), it is clear that a strong positive relationship exists between w and M, as expected. Even in the weaker updraft areas outside the main updraft, we see a correlation between w and M. But what does this correlation look like both mathematically and statistically?

Figure 2a shows a scatterplot of w versus M for $T_{env} = -25°$C to $T_{env} = -20°$C, encompassing the data in Fig. 1. In other words, Fig. 2a is the result of mapping data such as those shown in Figs. 1c,d onto a new (w, M) phase space. It is immediately apparent that a linear relationship between w and M appears to exist for this particular temperature range, albeit with variability for points primarily where $w < 10$ m s^{-1} and with several apparent linear fits at higher updraft speeds and rain-dominated
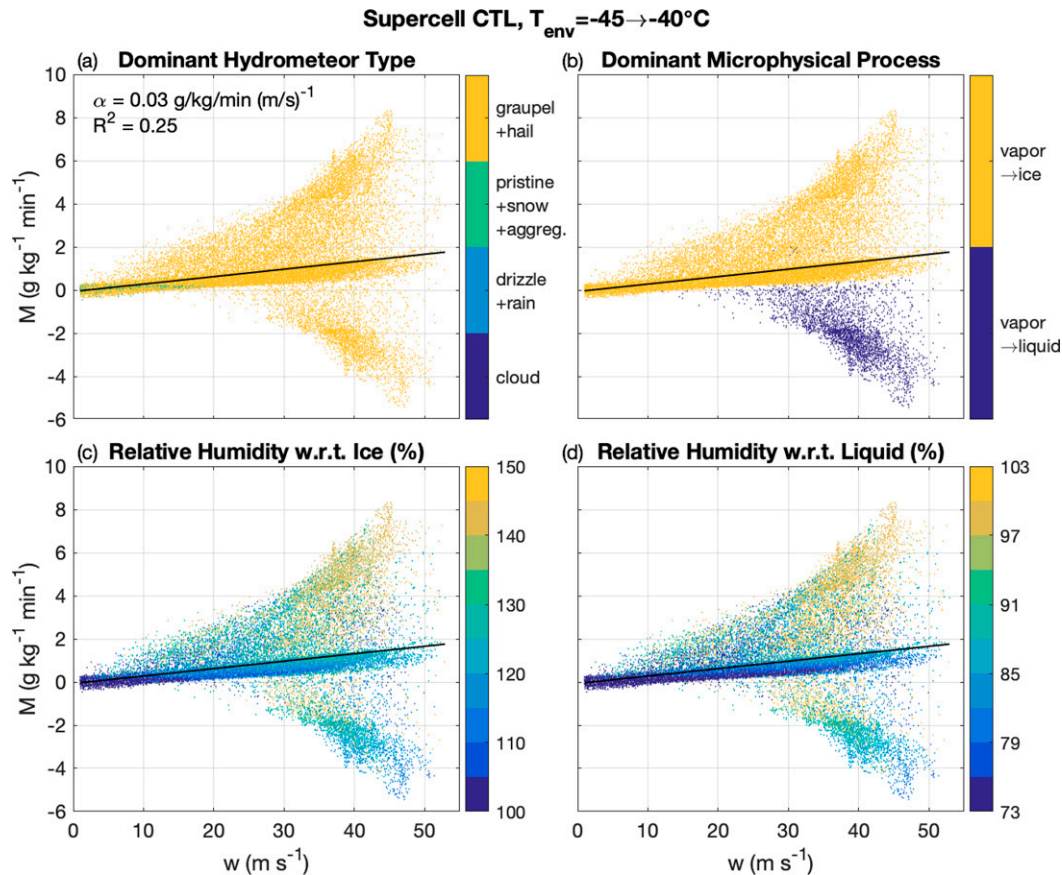
FIG. 3. Scatterplot and linear fit for the Supercell CTL case and the $-45°$ to $-40°C$ environmental temperature range. Results are as in Fig. 2a with dot colors indicating quantities labeled in the panel titles. In (b), vapor $\rightarrow$ ice indicates net values of deposition $-$ sublimation and vapor $\rightarrow$ liquid indicates net values of condensation $-$ evaporation $+$ cloud nucleation.

grid points. The variability at lower updraft speeds results from sampling regions of the storm anvil and cloud edges, while the multiple apparent linear fits at higher updraft speeds and rain-dominated grid points arise from the discrete model vertical levels. Despite this variability, the R^2 of the linear fit is 0.96 (Fig. 2a), indicating that the linear fit explains 96% of the variance in the relationship between w and M. The linear fit works well irrespective of whether liquid or ice hydrometeors are most prevalent, as shown by the different colors in the scatterplot, which is surprising because the supersaturation over liquid and ice at these temperatures can be substantially different. The linear fit also works well over different parts of the updraft.

The slope and R^2 of a linear fit between w and M for the entire temperature range of the supercell are shown in Figs. 2b,c. Several important points are evident from these results. First, the slope of the linear fit between w and M depends on T_{env} (and by extension pressure, since temperature and pressure are positively correlated in the environment). Specifically, we see smaller slopes of the linear fit at colder temperatures, and larger slopes of the linear fit at warmer temperatures. In fact, this temperature dependence explains the three apparent linear fits at higher updraft speeds and rain-dominant grid points in Fig. 2a, because there are three discrete model

vertical levels in the $-25°$ to $-20°C$ temperature bin. Second, the R^2 of the fit is generally large except at the temperature bins (i)–(iv) labeled in Fig. 2c, suggesting a strong linear relationship for many temperatures other than the $-25°$ to $-20°C$ bin shown in Fig. 2a. The R^2 is largest in the mixed-phase temperature regions ($-10°$ to $-30°C$).

The R^2 has a local minimum at four specific locations, labeled in Fig. 2c: (i) below cloud base at very warm temperatures; (ii) at cloud top; (iii) at the $-45°$ to $-40°C$ temperature range, where R^2 reaches its lowest value (0.25) except for below cloud base; and (iv) in the $-5°$ to $0°C$ temperature range. The poor fit at cloud top (point ii) is due to variability in M at low updraft speeds influenced by local fluctuations in supersaturation arising from cloud-top entrainment processes. The poor fit below cloud base (point i) results from falling precipitation below cloud base where the air is subsaturated and condensation rates are not well correlated with updraft speeds. We will next explore in more detail why R^2 is so strongly suppressed around $-40°C$ (point iii), which we know is close to the homogeneous freezing temperature for liquid water where cloud and rain drops will freeze without the aid of ice nucleating particles, and also discuss the local minimum in R^2 near the melting level (point iv).

Supercell CTL, $T_{env}=-5\rightarrow0°C$
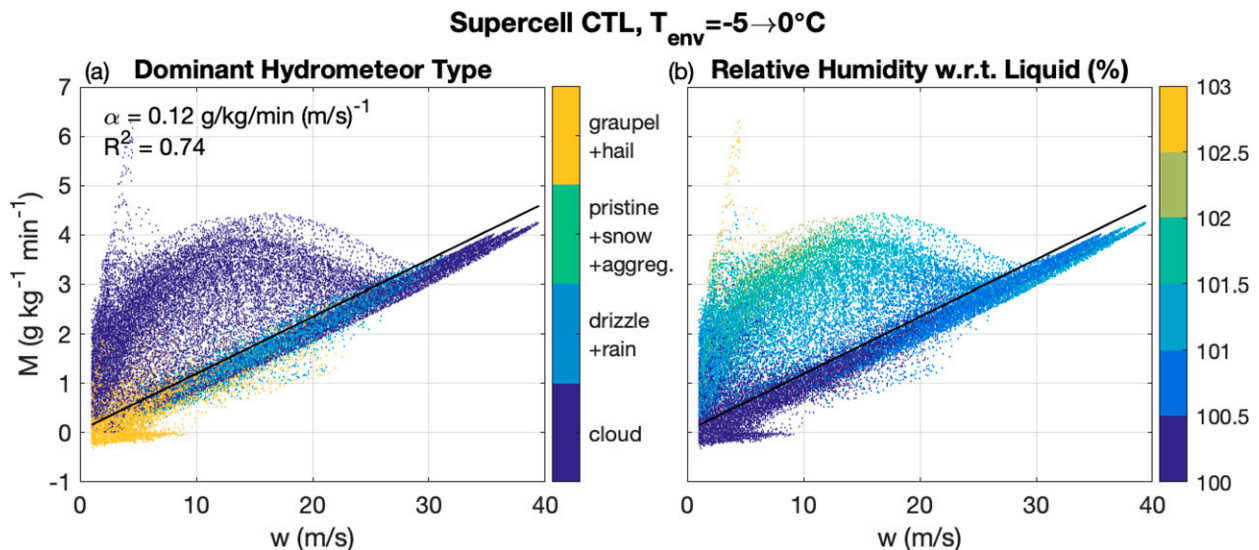

FIG. 4. (a) As in Fig. 3a and (b) as in Fig. 3d, but for environmental temperatures between −5° and 0°C. Note differences in color bar scale and axis scaling from Fig. 3.

Scatterplots of w versus M for the −45° to −40°C temperature interval are shown in Fig. 3. First, it is clear that scatter in the values of M for larger values of w (>10 m s^{-1}, or approximately the top 15% of updraft points in this temperature interval) leads to the low R^2 value at this specific temperature range. Ice hydrometeors are more prevalent than liquid water (Fig. 3a). This makes sense considering that the temperature range examined here is near the homogeneous freezing level. However, when looking instead at the dominant microphysical process in each grid box (Fig. 3b), it is clear that for similar updraft speeds (say, 40 m s^{-1}), the grid points with large positive values of M are characterized by high ice deposition rates, while the grid points with negative values of M are grid points dominated by high liquid evaporation rates. Thus, the scatter in the data at this temperature range is due to the Wegener–Bergeron–Findeisen process (WBF; Wegener 1911; Bergeron 1935; Findeisen 1938). In this process, ice particles forming in regions of primarily liquid water will grow at the expense of the liquid water when the vapor pressure is between that of the saturation vapor pressure over liquid and ice, since the saturation vapor pressure over ice is smaller than the saturation vapor pressure over liquid water. Stated another way, relative humidity over ice is higher than relative humidity over liquid, driving high deposition rates onto ice particles because supersaturation is the primary driver of condensation or deposition. The deposition rates are high enough that relative humidity is driven below liquid water saturation for some updraft points (Fig. 3d). It is evident from Figs. 3a and 3b that for this T_{env} range, most but not yet all of the liquid has already transitioned into ice, which is an expected result given that the temperatures are near the homogeneous freezing level.

To verify that the scatter in the −45° to −40°C temperature range is due to WBF, we examine the relative humidity with respect to ice (Fig. 3c) and to liquid (Fig. 3d). It is evident that the grid points with high ice deposition rates also have high

supersaturations with respect to ice (Fig. 3c), explaining the rapid ice particle growth. All updraft grid points at this temperature range are also ice-supersaturated, and thus we would expect to see ice particle growth at all values of w. However, many updraft grid points are liquid subsaturated in this temperature range due to rapid ice growth (Fig. 3d), especially the grid points characterized primarily by liquid evaporation (purple dots).[1] Taken together, the data shown in Fig. 3 suggest that the regions of poor R^2 for the linear fit between w and M are due to highly active liquid–ice phase change processes such as WBF, which can be active anywhere in the mixed-phase region depending on ice processes and the ice nucleating particles that are present, but which are especially active near the homogeneous freezing level.

Furthermore, the data in Fig. 3 indicate that the relationship between w and M is modulated by the relative humidity. This is evident from Fig. 3c and Fig. 3d: there is some scatter even in the high-density cluster of (w, M) points that the linear fit most closely approximates, with shallower slopes characterized by lower relative humidities and steeper slopes characterized by higher relative humidities. This fact is also evident in Fig. 4, which displays scatterplots of w versus M for the −5° to 0°C temperature interval. In this temperature range, we primarily see liquid water as expected (Fig. 4a). There is a clear linear relationship between w and M that is most closely approximated by the solid black line. There is also an arc of high values of M which are comprised primarily of cloud droplets (purple dots in Fig. 4a). In this arc, we see a

---

[1] Some of the grid points characterized by liquid evaporation also show supersaturations with respect to liquid. This is because M is accumulated over a 1-min interval but relative humidity is an instantaneous value, thus reflecting rapid temporal fluctuations in supersaturation. These fluctuations can be expected near the homogeneous freezing level, particularly for a supercell with extreme turbulence.
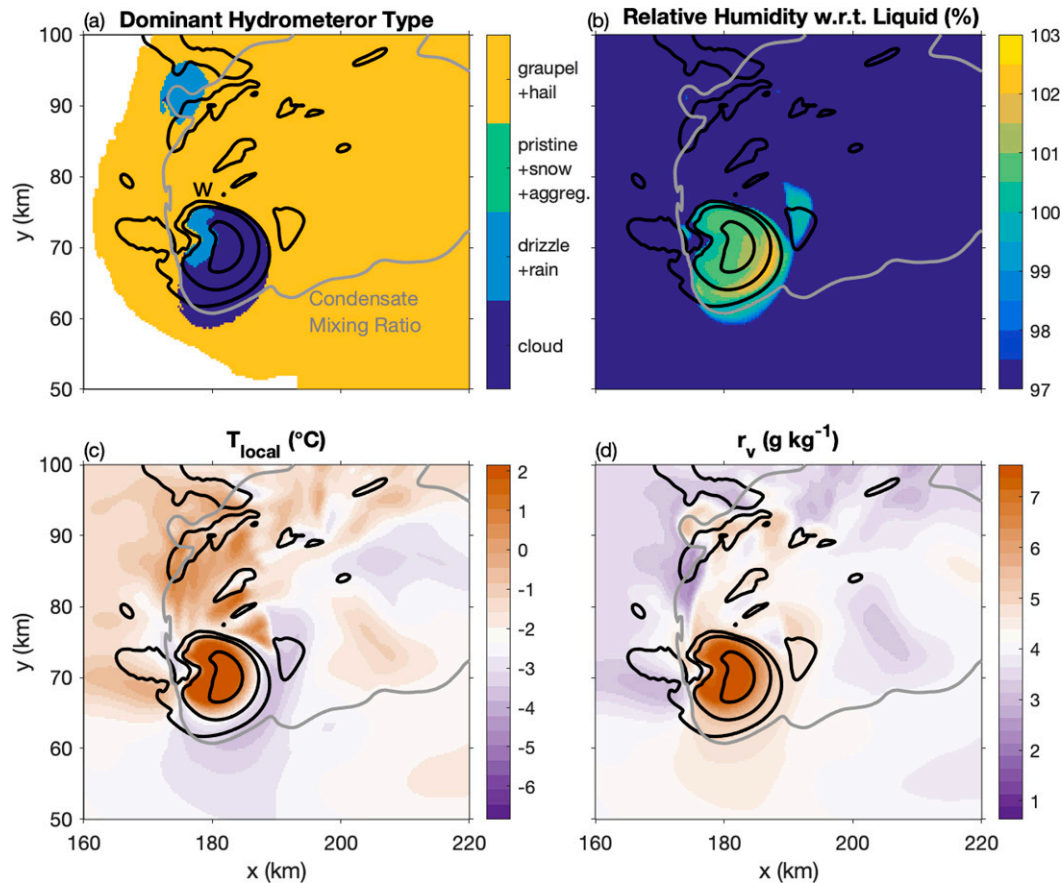
FIG. 5. Snapshots of (a) hydrometeor type with the largest mixing ratio in each grid box, (b) relative humidity with respect to liquid water, (c) temperature, and (d) water vapor mixing ratio for the Supercell CTL case. Results are shown at approximately 4 km AGL where T_{env} is $-2.3°C$. The 0.1 g kg^{-1} total condensate is contoured in gray and $w = 1, 10,$ and 30 m s^{-1} are contoured in black. Color bars in (c) and (d) are centered on the environmental values at this altitude.

relative humidity dependence: the relative humidities with respect to liquid water are higher than relative humidities in the main linear fit region, and the very highest condensate growth rates in this arc occur in conditions of liquid supersaturations of up to 3% (Fig. 4b). Thus again, the relative humidity modulates the relationship between w and M.

Finally, we ask what causes the higher relative humidity near the freezing level leading to the arc of departure from the linear relationship seen in Fig. 4? An example image from the Supercell CTL case is shown in Fig. 5. The highest supersaturations are found in the southeast portion of the main updraft (Fig. 5b) which is comprised of primarily cloud water (Fig. 5a) and moderate 10–20 m s^{-1} updraft speeds. This region of the updraft is cooler (Fig. 5c) and drier (Fig. 5d) than the rest of the updraft, and even cooler than the environmental temperature at this altitude. This edge of the updraft reflects deep-layer inflow into the supercell. The temperatures are cooler and drier due to adiabatic ascent in the elevated inflow that does not have a history of latent heating like the air in the deeper core of the updraft, which originated in the boundary layer. The deep-layer inflow can be seen in Fig. 8 of Grant and van den Heever (2014) and is a common feature of all types of deep convection

(e.g., Mechem et al. 2002; McGee and van den Heever 2014; Schiro et al. 2018). This analysis suggests two interesting points: 1) the strongest updrafts do not contain the greatest supersaturation, in contrast to earlier references that suggested a linear relationship between w and supersaturation in studies of mostly liquid clouds and more benign updrafts (e.g., Squires 1952; Politovich and Cooper 1988); and 2) the deep-layer inflow results in enhanced supersaturations which maximize near the melting level. This finding, along with microphysical impacts of freezing and melting on temperatures and supersaturations near the melting level, explains the gradually decreasing correlations from ~15° to $-5°C$ at point (iv) (Fig. 2c).

b. Relationship between w and M for all simulations

We have thus far examined the relationship between w and M over a range of environmental temperatures for a supercell case and found that a linear regression well explains the relationship between w and M, except near active phase change regions, below cloud base, and at cloud top. We next ask, do these results hold for different types of convection and for different environments? Do they vary if we consider environmental temperatures (T_{env}) or in-cloud temperatures (T_{local})? And do the results
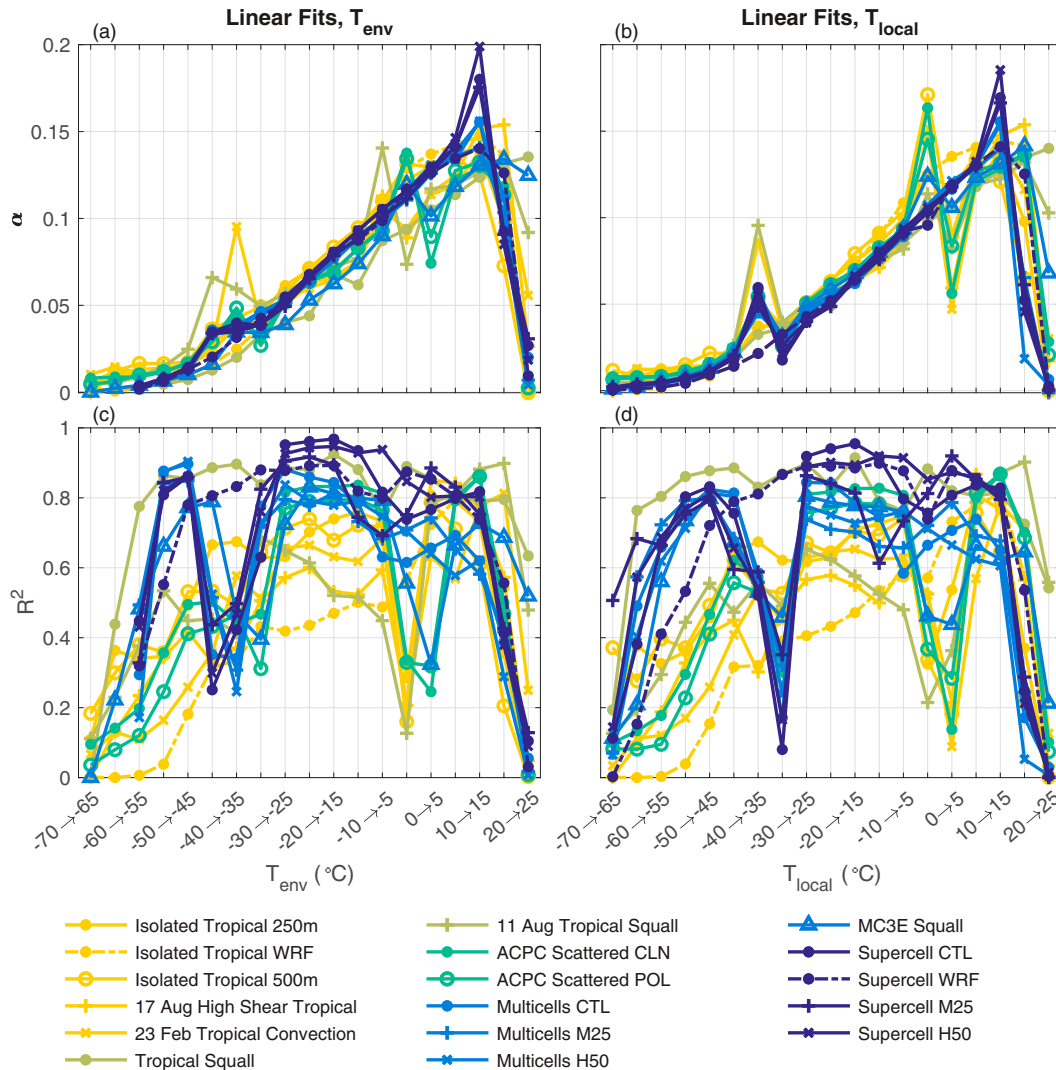
FIG. 6. (a),(b) Slope and (c),(d) R^2 of the linear fit between w and M as a function of (a),(c) environmental temperature (T_{env}) and (b),(d) local, in-cloud temperature (T_{local}) for the entire simulation suite. Colors indicate groupings of convective types from warmest colors (unorganized tropical cases) to coolest colors (organized midlatitude cases). Dash–dotted lines indicate WRF simulations.

depend on the model platform or are they specific to the RAMS microphysics scheme used in the Supercell CTL case?

The slope and R^2 of the linear fit between w and M for 5°C T_{env} bins and for every case of the model ensemble listed in Table 1 are shown in Figs. 6a and 6c. The slope of the linear fit is consistent among the simulation suite, considering the wide variety in types of convective environments (tropical, midlatitude, maritime, continental, polluted, clean), convective organization (short-lived single-cells, squall lines, and convective clusters), and model platforms (RAMS and WRF-Morrison). For instance, the WRF Morrison slope results fall in the range of the RAMS results. There are a few outliers in slopes near the freezing level and homogeneous freezing level for specific simulations including the 11 Aug Tropical Squall, the 23 Feb Tropical Convection, and the two ACPC cases. The R^2 of the linear fit (Fig. 6c) have

values generally above 0.6 in the mixed-phase temperature range, and between cloud base (which varies among the cases) and the freezing level, although with more variability than the slope results. There is also variability in the T_{env} bins where the R^2 reaches its local minima near the freezing and homogeneous freezing levels. It is apparent from the warm-to-cool color progression in Fig. 6 that the R^2 increases from unorganized tropical convection (smallest R^2) to organized midlatitude convection (largest R^2). This is particularly true in the mixed-phase temperature range but also in the ice and warm phases of the convection. The results in Fig. 6 suggest that the physics related to the fast time scales for adjustments in supersaturation as discussed in previous studies (e.g., Squires 1952; Politovich and Cooper 1988) are applicable to many portions of deep convection, despite the presence of intense updrafts, fast accelerations, large

precipitating liquid and ice hydrometeors, and extreme turbulence, even though the highest supersaturations are not necessarily collocated with the strongest updrafts (Fig. 5b) in contrast to findings in the earlier studies.

In-cloud temperatures can depart considerably from environmental temperatures, especially for stronger updrafts that are associated with more latent heating, thus leading to variability in the in-cloud temperature perturbations among the different types of convection represented in the ensemble. We may therefore expect to see less variability in the slope and R^2 results across the ensemble if the results were binned by T_{local} rather than T_{env} because T_{local} represents the conditions at each individual grid point that the hydrometeors experience. Indeed, this is the case: the slope and R^2 results for the linear fit as a function of T_{local} are shown in Figs. 6b and 6d, and it is clear that the variability in the slope among the simulations is reduced when binned by T_{local} instead of T_{env} (cf. Figs. 6a and 6b). Further, the temperature bins where the R^2 minima near the freezing and homogeneous freezing levels are located do not vary as much for the T_{local} results compared to the T_{env} results (cf. Figs. 6c and 6d). The reduced variability in the slopes and the temperature locations of the R^2 minima are expected, since in-cloud temperature represents the local in-cloud conditions at which the w–M relationship is examined. However, a natural cool-to-warm color progression is still evident in Figs. 6b and 6d, showing higher R^2 and slightly smaller slopes for organized midlatitude cases, and lower R^2 and higher slopes in unorganized tropical cases, which may be related to differences in entrainment into the updraft core. Even so, it is clear that there is significant similarity among the various simulations, even when T_{env} is used as the determining factor in place of T_{local}.

Interestingly, two cases have consistently high R^2 values even near the freezing and homogeneous freezing levels in both the T_{env} and T_{local} results: Supercell WRF Morrison and the Tropical Squall (Figs. 6c,d). It is not clear why the Tropical Squall case has a higher R^2 than many other cases, although it does notably have a small relative minimum in R^2 near the freezing and homogeneous freezing levels. On the other hand, the Supercell WRF Morrison case does not have a local R^2 minimum near the homogeneous freezing level. The two WRF Morrison cases use the Morrison microphysics scheme (Morrison et al. 2005, 2009) which applies saturation adjustment, following the setup of the WRF Model framework and similar to other WRF bulk microphysics schemes (Skamarock et al. 2019), whereas the RAMS microphysics scheme predicts supersaturation. We conjecture that the poor correlation near the homogeneous freezing level, shown explicitly for the RAMS Supercell CTL case due to WBF (Fig. 3), is a realistic impact of modeling supersaturation and its resulting modulation of the w–M relationship, and that these subtleties cannot be captured using a microphysics scheme with saturation adjustment in which the excess water vapor (above saturation) is forced to condense each time step.

To verify this point, we created the scatterplots at the homogeneous freezing level (Fig. 3) for the WRF Supercell Morrison case, which are shown in Fig. 7. For both RAMS and WRF, the dominant hydrometeor types are ice particles (Fig. 3a and Fig. 7a), as expected for deep convection where $T_{env} < -40°C$. However, the effect of saturation adjustment in the WRF Morrison scheme becomes obvious in the remaining panels. Because supersaturation with respect to liquid water is removed during saturation adjustment, most of the updraft data points are at saturation or are close to it (Fig. 7d), in contrast to the results from the RAMS microphysics scheme (Fig. 3d). The Morrison scheme allows supersaturation with respect to ice to remain, resulting in values above 100% in Fig. 7c. The saturation adjustment does not allow explicit representation of water vapor competition in the WBF process, which is evident in Fig. 7b. Even at $-40°C$, condensation dominates over vapor deposition, which is the opposite result to the RAMS simulations (Fig. 3b). Condensation dominates because the saturation adjustment, combined with the prescribed cloud droplet number in the Morrison scheme, forces cloud droplets to activate and grow by condensation until the relative humidity is at or below saturation with respect to liquid water. Then the newly activated and grown cloud drops homogeneously freeze into cloud ice (given the temperatures colder than the homogeneous freezing level), and finally grow by vapor deposition.[2] Thus, the overall effect of the saturation adjustment is to artificially enhance the R^2 value for this temperature range in WRF.

Overall, the results of this section suggest that a *simple linear relationship* between w and M is a good approximation within deep convective clouds except near the freezing and homogeneous freezing levels. The linear relationship is defined as follows:

$$M = \alpha(T)w, \qquad (5)$$

where α *is the slope of the linear fit between w and M and is only a function of temperature*, either environmental or in-cloud (see also van den Heever et al. 2018 and Stephens et al. 2020). Although the T_{local} results are more consistent across the ensemble, the correlations with T_{env} are nevertheless highly useful because T_{env} is more easily obtained through reanalysis, targeted radiosondes, or satellite sounders compared to local spatially and temporally variable in-cloud temperatures. Therefore, for the remainder of this paper, we will use T_{env} in Eq. (5). The importance and implications of Eq. (5) are next discussed.

5. Implications of the w–M relationship

A linear relationship between w and M is of interest for a number of reasons. First, this relationship, obtained from full physics cloud-resolving model simulations, may assist in advancing our theoretical understanding of the links between cloud physics and cloud dynamics, as well as processes driving convective mass fluxes, transport, and precipitation. We discussed above (section 2) that it is difficult to assess the relationships between vertical velocity and microphysical processes in Eqs. (3) and (4), or indeed relationships between other terms in these equations, because they are highly nonlinear and coupled, and deep convective processes such as precipitation-size liquid and ice hydrometeors, rapid vertical accelerations, and extreme turbulence make application of simplifications

---

[2] Condensation at temperatures colder than the homogeneous freezing level has also been seen in other studies using WRF and saturation adjustment microphysics schemes (Heikenfeld et al. 2019).
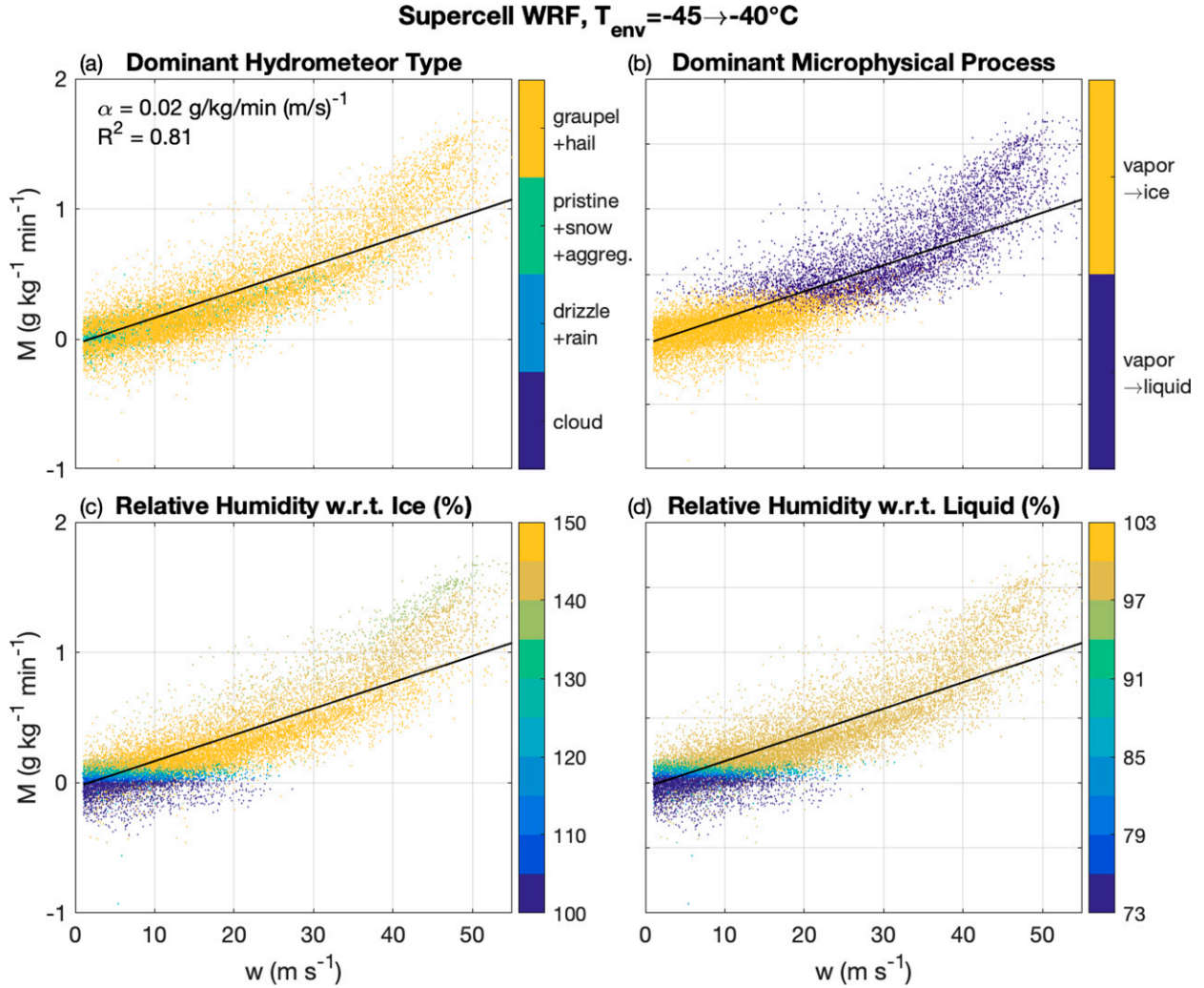
Supercell WRF, $T_{env}=-45\rightarrow-40°C$

FIG. 7. As in Fig. 3, but for the Supercell WRF case. Note the different y axes here as compared to Fig. 3.

from prior studies of cloud droplets and small ice crystals for clouds with more benign updrafts difficult to apply. However, knowledge of the linear relationship between w and M obtained here for deep convection can illuminate simplifications that can be made in these prognostic equations and lead to additional relationships and insights about cloud microphysical-dynamical links. Second, since both w and M are notoriously difficult to observe, knowledge of the linear relationship between them may have applications for future observing systems. It is this latter possibility that we next explore.

Recall that Eq. (4) is the tendency equation for the condensed water mixing ratio r_c, and that w and M both appear on the right-hand side of this equation. Substituting Eq. (5), the linear relationship between w and M, into Eq. (4), we obtain the following:

$$\frac{\partial r_c}{\partial t} = -\mathbf{U}_h \cdot \mathbf{V}_h r_c - [w - v_t]\frac{\partial r_c}{\partial z} + \alpha(T_{env})w + D, \quad (6)$$

where w appears twice on the right-hand side of Eq. (6), and so this equation can be rearranged to solve for w:

$$w_{diag} = \frac{\frac{\partial r_c}{\partial t} + \mathbf{U}_h \cdot \mathbf{V}_h r_c - v_t\frac{\partial r_c}{\partial z} - D}{\alpha(T_{env}) - \frac{\partial r_c}{\partial z}}, \quad (7)$$

where w has been replaced by w_{diag} because Eq. (7) forms a diagnostic equation for vertical velocity [see Stephens et al. (2020) for discussion of this equation in terms of radar reflectivity]. In Eq. (7), the first term in the numerator represents the condensate tendency term, the second the horizontal advection term, the third the sedimentation term, and the fourth the diffusion term. The denominator on the right side of Eq. (7), $\alpha(T_{env}) - \partial r_c/\partial z$, is a scaling factor for each term in the numerator.

Equation (7) is of significance because if the terms on the right-hand side of Eq. (7) were known or could be measured, then vertical velocity could in theory be diagnosed. Note that Eq. (7) does not contain any explicit representation of microphysical processes, which are perhaps the most difficult to observe, whereas horizontal and vertical gradients
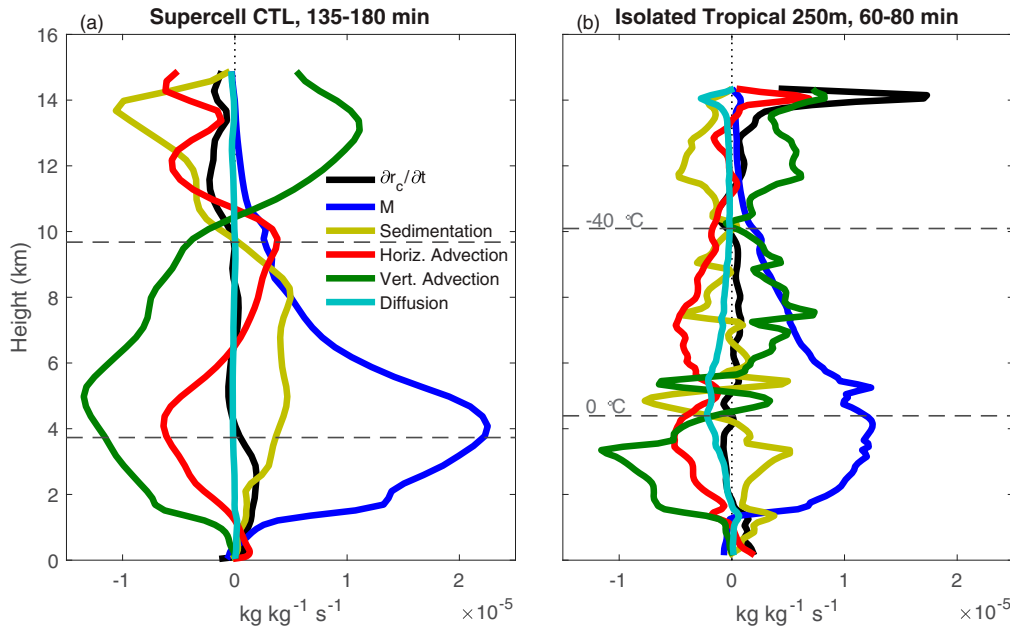
FIG. 8. Profiles of mean contributions to the condensate tendency equation [Eq. (4)] for (a) the Supercell CTL case and (b) the mature stage of the Isolated Tropical 250m case. Budget terms are averaged over all grid points where $w > 1$ m s^{-1} and $r_c > 0.1$ g kg^{-1}, and in time as labeled in each title. Mean budgets are smoothed in the vertical using a three-point triangular filter to eliminate gridscale noise. The values of $T_{env} = 0°$ and $-40°$C are shown in dashed gray lines.

in condensate mixing ratio and horizontal winds are arguably easier to obtain. Finally, if assumptions can be made about sedimentation velocities and diffusion, and since $\alpha(T_{env})$ is obtained from the simulation results [Eq. (5) and Fig. 6a], then Eq. (7) provides a viable framework for diagnosing vertical velocity.

How well does the diagnosed vertical velocity obtained from Eq. (7) match the true vertical velocity, given that the microphysical process rate assumption [Eq. (5)] has been used to obtain Eq. (7)? To answer this question, we first look at the terms in the condensate tendency equation [Eq. (4)], since the condensate tendency equation is the underlying basis for obtaining Eq. (7) and diagnosing w. Each term in Eq. (4) was estimated from the model output using second-order centered finite differencing. The computed terms were then averaged over cloudy updraft points in order to examine the average relative magnitudes of each term. [The RAMS code was also modified to exactly output each term in Eq. (4), and the Isolated Tropical 500m case was simulated with this modified code. The finite difference approximations to the terms in Eq. (4) were compared to the exact terms, and the approximations were found to be sufficiently accurate; not shown.] Results from this analysis are displayed in Fig. 8 for two different simulations that represent the opposite ends of the spectrum of convective organization and environments: the Supercell CTL case and the Isolated Tropical 250m case. The averaging times in both cases encompass the mature stage of the storm for a fair comparison (the Supercell CTL case is in a quasi–steady state, and the 45-min time period represented in the average includes all times for which 1-min model output is available).

In both cases, the condensate tendency (black lines) is small throughout most of the cloud depth, in keeping with the fact that both storms are analyzed during their mature stages. Further similarities between the two include a large positive contribution to condensate tendencies by microphysical processes M (blue lines) in the lower half of the updrafts, and negative (positive) contributions to condensate tendencies by vertical advection (green lines) in the lower (upper) portions of the updrafts. The vertical advection results are as expected considering the budgets are averaged over updraft points, and updrafts transport condensate from the lower to upper portions of the cloud, thus decreasing condensate mixing ratios in the lower part of the cloud and increasing them in the upper part. Sedimentation (gold lines) is also an important contributor to condensate tendencies and tends to be of opposite sign to the vertical advection: sedimentation decreases condensate mixing ratios in the upper portions of the updraft and increases condensate in the lower portions of the updraft, as expected in mature precipitating systems. Horizontal advection (red lines) can be large and varies in sign throughout the depth of the cloudy updrafts, while diffusion (cyan lines) is negligible as expected, although we include diffusion in the remainder of the analysis in this paper for completeness. In the lower portion of the cloud, vertical advection and condensation processes are the largest terms in magnitude and are of opposite sign, suggesting that M may be the only process with fast-enough time scales to approximately balance the vertical advection in strong updrafts, which agrees with earlier studies (e.g., Squires 1952; Paluch and Knight 1984). Above the freezing level and in the upper portions of the cloud, however, M and vertical advection are not well balanced,
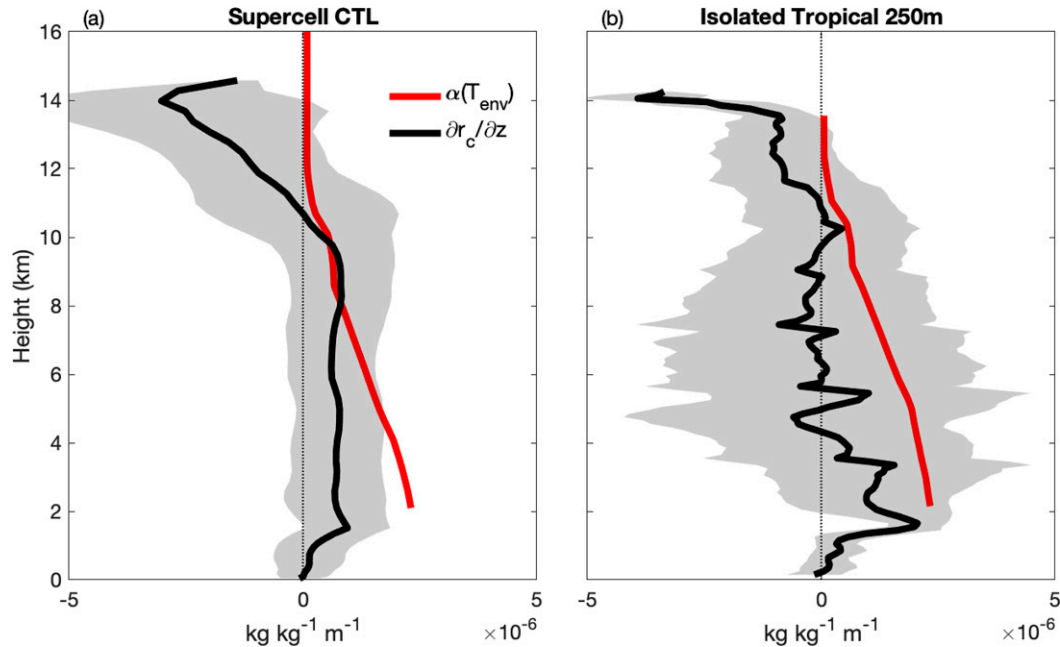
FIG. 9. Vertical profiles of median corrected $\alpha(T_{env})$, interpolated to the environmental temperature at each altitude (see text for details), and mean (solid black lines) plus and minus one standard deviation (shaded) of the vertical profile of $\partial r_c/\partial z$ for (a) the Supercell CTL case and (b) the mature stage of the Isolated Tropical 250m case. Horizontal averages and standard deviations of $\partial r_c/\partial z$ at each altitude and time were determined for points where $w > 1$ m s^{-1} and $r_c > 0.1$ g kg^{-1}, and then averaged over the same times as in Fig. 8.

which may be related to the slower time scales associated with deposition adjustments to supersaturation for ice particles (e.g., Korolev and Mazin 2003). In general, the magnitude of condensate tendency terms are stronger in the Supercell CTL case (Fig. 8a) than in the Isolated Tropical 250m case (Fig. 8b), since the supercell convection is more intense than the isolated tropical convection. Finally, the isolated tropical convection results are noisier than the supercell results because the isolated tropical convection is more transient, has a smaller updraft overall, and its mature stage lasts for a shorter amount of time than the sustained, well-organized supercell updraft.

Now that we have a sense of the magnitude of the various terms that contribute to the temporal changes in condensate mixing ratio, how well does Eq. (7) diagnose the model's true w? To estimate w_{diag} using Eq. (7), the median slope among the suite of simulations is used for $\alpha(T_{env})$. The median is chosen to avoid the influence of outliers at certain temperatures (Fig. 6a). Two corrections are then made to $\alpha(T_{env})$. First, an artificial jump occurs in the value of $\alpha(T_{env})$ from the $-65°$ to $-60°$C bin to the $-60°$ to $-55°$C bin, because only half of the simulations produce values of $\alpha(T_{env})$ at the lowest two temperature bins (from $-70°$ to $-60°$C). Therefore, the value of $\alpha(T_{env})$ for the $-65°$ to $-60°$C bin is replaced by the average of the $-70°$ to $-65°$C and $-60°$ to $-55°$C bins. Second, $\alpha(T_{env})$ begins to decrease at environmental temperatures warmer than 15°C because these temperatures are in the subcloud layer for many of the simulations. However, in reality, we expect $\alpha(T_{env})$ to increase with increasing temperature, as it does for the Tropical Squall case (Figs. 6a,b), which has

much warmer cloud base temperatures than the other cases. Therefore, we only define $\alpha(T_{env})$ for environmental temperatures colder than 15°C. The values of $\alpha(T_{env})$ are assumed to be valid at the midpoint of the 5° temperature bins and are linearly interpolated to the environmental temperature at each height for each case. The vertical profiles of $\alpha(T_{env})$ as a function of height for both the Supercell CTL and Isolated Tropical 250m cases are shown in Fig. 9 (red lines). The profiles of $\alpha(T_{env})$ look different for the two cases because the two cases have different environmental temperature profiles.

Another consideration for estimating w_{diag} from Eq. (7) is that Eq. (7) cannot be used where the denominator is small, i.e., when $\alpha(T_{env})$ and $\partial r_c/\partial z$ are of similar magnitude and of the same sign. Profiles of the mean and standard deviation of $\partial r_c/\partial z$ are also shown in Fig. 9 for both cases. Based on the overlap between $\alpha(T_{env})$ and the standard deviation of $\partial r_c/\partial$, there are regions throughout the cloudy updraft that do meet this criterion and thus portions of the updrafts where we cannot calculate w_{diag} using Eq. (7). In the subsequent analysis, we only present w_{diag} where the denominator of Eq. (7) exceeds a tolerance of 1×10^{-7} kg kg^{-1} m^{-1}. This tolerance was subjectively chosen to both minimize noise and include as many updraft points as possible in the analysis.[3]

_____

[3] Different values were tested for the denominator: 1×10^{-6} kg kg^{-1} m^{-1} was found to be too restrictive, whereas 1×10^{-7} kg kg^{-1} m^{-1} was found to be much less restrictive but can produce noisy profiles. This explains some of the noise that can be seen in Fig. 10b.

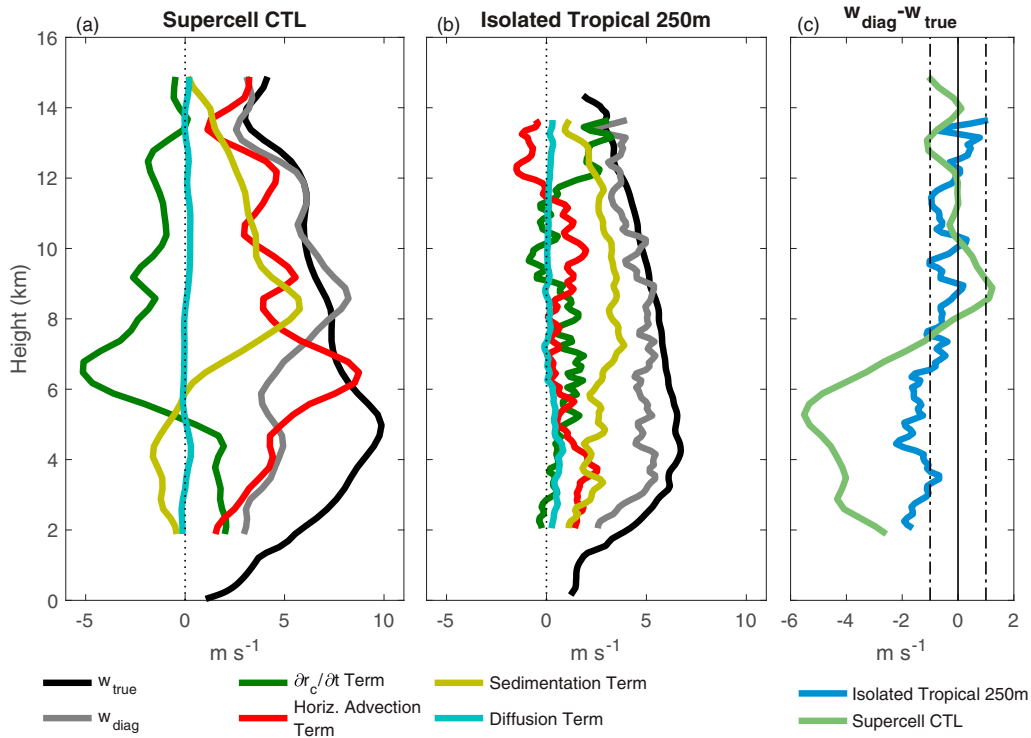FIG. 10. Plots of w_{true} vs w_{diag} obtained using Eq. (7), and the terms in the numerator of Eq. (7) contributing to w_{diag} all scaled by the denominator to give units of m s^{-1}, for (a) the Supercell CTL case and (b) the mature stage of the Isolated Tropical 250m case. The w_{true}, w_{diag}, and individual terms are averaged over grid points where $w > 1$ m s^{-1}, $r_c >$ 0.1 g kg^{-1}, and where the Eq. (7) denominator exceeds 1×10^{-7} kg kg^{-1} m^{-1}, and over the same times as in Figs. 8 and 9. Terms are smoothed in the vertical using a three-point triangular filter to eliminate gridscale noise. (c) The difference between the mean profiles of w_{diag} and w_{true} for both cases, with ± 1 m s^{-1} shown by dash–dotted lines.

Figures 10a and 10b show averaged profiles of the model's true vertical velocity (w_{true}) compared to w_{diag} obtained from Eq. (7) for each case. Each term that contributes to w_{diag}, scaled by $\alpha(T_{\text{env}}) - \partial r_c/\partial z$, is also shown in Figs. 10a and 10b. The results demonstrate that the temporal change in condensate and the horizontal advection terms are important near cloud top, the sedimentation term is an important contributor to w_{diag} throughout the middle depth of the cloud, and diffusional contributions are small and can be safely neglected as expected. Most importantly, Fig. 10c shows differences between the averaged w_{diag} and w_{true} for both cases and reveals that w_{diag} falls within 1 m s^{-1} of w_{true} in the upper half of the cloud, although w_{diag} tends to underestimate w_{true} in the lower half of the updrafts, particularly for the supercell, largely due to errors in approximating the microphysical term [$\alpha(T_{\text{env}})$]. Given the magnitude of this term in the lower portion of the cloud (Fig. 8), and the lower R^2 at these altitudes particularly for the supercell case (Fig. 2c), we might expect larger errors in w_{diag}. However, the agreement between w_{diag} and w_{true} in the upper half of the cloud is quite encouraging, pointing to the utility of the diagnostic equation using measurements from the top of the cloud (e.g., satellite-based).

Finally, plan views showing the model's instantaneous w_{true}, w_{diag}, and the various terms contributing to w_{diag} are displayed

in Fig. 11 to obtain a sense of how well the diagnostic w equation [Eq. (7)] behaves in different spatial regions of the cloud. Results are shown for the Supercell CTL case at 7.5 km AGL (T_{env} is -22.5°C; results are similar at other altitudes and temperatures, not shown). By comparing w and w_{diag} directly (Figs. 11a–c), it is clear that w_{diag} correctly captures the main updraft's shape and spatial structure of horizontal gradients in w_{true} within the updraft core. However, w_{diag} slightly underestimates the magnitude of w_{true} in the core (Fig. 11c). This is because $\alpha(T_{\text{env}})$ is based on the environmental temperature, but in the updraft core, in-cloud temperatures are warmer than surrounding environmental temperatures due to latent heating. We confirmed this explanation by creating Fig. 11 except using $\alpha(T_{\text{local}})$ instead of $\alpha(T_{\text{env}})$ in Eq. (7) (not shown). This also partly explains why $w_{\text{diag}} - w_{\text{true}}$ is negative in the lower half of the updrafts on average (Fig. 10c) and why the supercell case has larger negative values than the isolated tropical case: the supercell case has stronger updrafts overall, and therefore more latent heating and larger temperature perturbations in the updraft core. There are also regions near the edge of the main updraft and in the weak regions of ascent north, east, and southeast of the main updraft (Fig. 11a) where w_{diag} does not perform as well (Figs. 11b,c). In these regions, the denominator of Eq. (7), $\alpha(T_{\text{env}}) - \partial r_c/\partial z$, is near
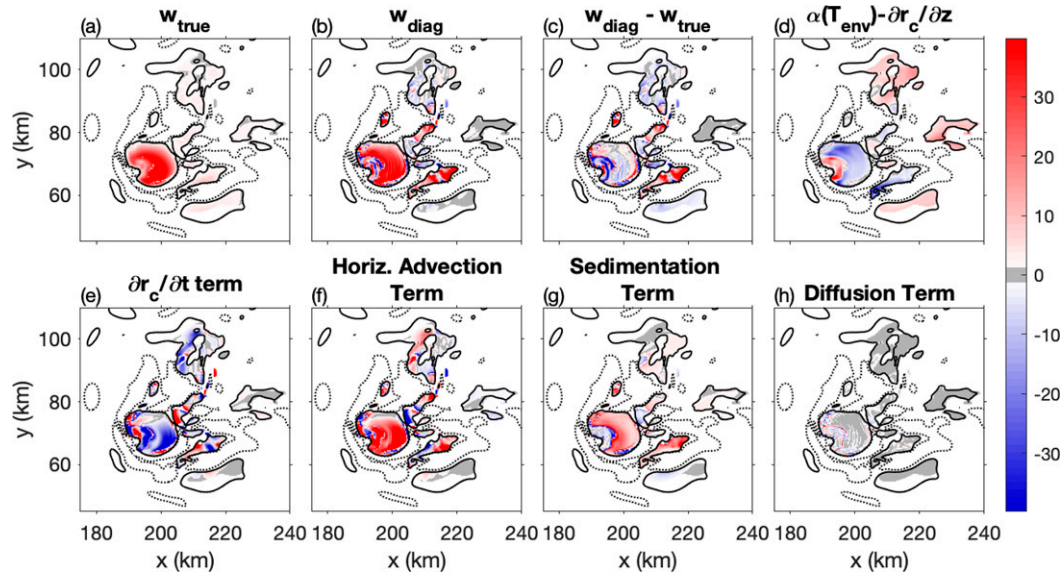
FIG. 11. Plan views of terms in the diagnostic w equation [Eq. (7)], as labeled in each panel title, for the Supercell CTL case at 7.5 km AGL ($T_{env} = -22.5°C$) and simulation minute 150. (a)–(c),(e)–(h) Values are only shaded for regions where $w > 1$ m s^{-1}, $r_c > 0.1$ g kg^{-1}, and $\alpha(T_{env}) - \partial r_c/\partial z > 1 \times 10^{-7}$ kg kg^{-1} m^{-1}; (d) regions are shaded where $w > 1$ m s^{-1} and $r_c > 0.1$ g kg^{-1}. The $+1$ (-1) m s^{-1} contours of w_{true} are shown in solid (dotted) black lines. All panels have units of m s^{-1}, except (d), which has units of 10^{-7} kg kg^{-1} m^{-1}.

zero or changes sign (Fig. 11d) which causes large positive and negative contributions to w_{diag} by the condensate tendency, horizontal advection, and sedimentation terms (Figs. 11e–g), although the diffusion term contribution is always small as expected (Fig. 11h). Despite these errors, w_{diag} still does well overall and especially when compared to w_{true} in a composite or averaged sense (Fig. 10). The performance of w_{diag} compared to w_{true} improves further if $\alpha(T_{local})$ is used in Eq. (7) instead of $\alpha(T_{env})$ (not shown). This suggests that techniques to estimate differences between T_{local} and T_{env}, such as the study by Luo et al. (2010) who used satellite observations of cloud-top temperature and height, cloud profiling, and soundings to estimate updraft buoyancy, could improve estimates of w_{diag}.

6. Summary

The importance of understanding vertical velocities in deep convection and its links to microphysical processes cannot be overstated. Deep convective vertical velocities and microphysical processes have impacts ranging from transport of water and mass throughout the troposphere and lower stratosphere, to the generation of severe weather and extreme precipitation and impacts on the global circulation (Cotton et al. 1995; Doswell et al. 1996; Riehl and Malkus 1958). The overarching goal of this study has been to determine the functional form of the relationship between vertical velocity (w) and microphysical process rates that convert water vapor into condensed water (M) in deep convection. To address this goal,

we examined a suite of high-resolution simulations of deep convection. The simulation ensemble spanned a range of environments including tropical oceanic, tropical continental, and midlatitude continental, relatively clean and polluted aerosol conditions, and a variety of convective organizational modes including single-cell short-lived convective towers, multicellular convective systems, squall lines, and supercells. Both idealized and case study simulations were included in the suite. Finally, different modeling platforms and microphysical schemes were also represented, resulting in an extensive dataset for examining relationships between vertical velocity and microphysical processes, and thereby enhancing the robustness of the findings. In addition to the diverse microphysics representations and storm morphologies, and in contrast to previous studies, we examine the full suite of condensation processes from liquid through mixed phase to ice-only, spanning the depth of deep convective systems.

The results from the ensemble of simulations showed that the relationship between w and M is robustly linear over a broad range of temperatures and storm types. The slope of the linear fit between w and M was found to be a strong function of temperature and secondarily a function of relative humidity. The slope was consistent among the simulations despite the wide variety of environments, convective organizational modes, and different modeling platforms and microphysics schemes represented. The R^2 of the linear fit was above 0.6 throughout the cloud depth except near regions in which liquid–ice phase changes are especially active (the freezing and homogeneous freezing temperatures) and near cloud base and cloud top. The R^2 was reduced near the

homogeneous freezing level because of the Wegener–Bergeron–Findeisen process, while the reduction in R^2 near the freezing level was found to be related both to deep-layer inflow to the convection and to freezing and melting processes. The slope and R^2 of the linear fit were more consistent when the w–M relationship was examined as a function of local in-cloud temperature (T_{local}) rather than environmental temperature (T_{env}), though the differences are in practice minor. We expect that the relationship as a function of T_{env} would be used in practice for spaceborne observational platforms because it far more straightforward to measure than T_{local}. The final proposed simple relationship between w and M, given by Eq. (5), includes the slope only as a function of temperature to a first-order approximation.

The linear relationship was then substituted into the condensate tendency equation and rearranged to form a diagnostic equation for w [Eq. (7)]. This diagnostic w equation offers a powerful theoretical framework for obtaining vertical velocity and hinges on the assumption that the other terms, which include temporal changes, horizontal gradients, and vertical gradients in condensate mixing ratio, sedimentation rates, and diffusional effects can be measured and/or neglected. The diagnostic equation was tested using the model output to examine its performance relative to the model's true w. Results showed initial promise: the storm-scale updraft speeds were able to be diagnosed within 1 m s^{-1} throughout the upper half of the clouds for two very different convective cases, a midlatitude supercell and a single-cell tropical continental tower. This is despite the use of the simple linear relationship between w and M with the slope of the relationship being only a function of T_{env}. Diffusional effects in the diagnostic w equation could safely be neglected. In the model, the sedimentation term was known exactly, which reduced the uncertainty in the diagnosed w. Sedimentation assumptions from observations and their impacts on diagnosed w require further investigation in future studies.

The linear relationship between w and M [Eq. (5)] and the diagnostic w equation [Eq. (7)] can be used to advance our understanding and observations of cloud physics and dynamical processes. We showed that the diagnostic w equation performs best in the upper half of the clouds, which suggests space-borne observations of the terms in the diagnostic w equation could be beneficial. Convoys of small satellites such as CubeSats are being increasingly utilized (e.g., Stephens et al. 2020); such satellites can provide the high (<1 min) temporal resolution measurements required for constraining estimates of w using techniques described in previous studies (e.g., Haddad et al. 2017; Sy et al. 2017). More generally, there has not yet been any satellite platform capable of measuring quantities related to the microphysical processes within clouds at sufficiently small time intervals to provide information on the time evolution of cloud microphysics or dynamics. It is possible that convoys of active and/or passive microwave instruments may provide such information in the future. If so, they will provide unprecedented information on the dynamic and microphysical processes and the links between them in storms. These are exciting avenues for future convective storms research.

Data availability statement. All simulation data used in this study are documented in previously published manuscripts as detailed in Table 1. A repository containing the namelists for all simulations is available at http://dx.doi.org/10.25675/10217/233963 (Grant et al. 2021). For simulation output data, contact R. Storer (rachel.l.storer@jpl.nasa.gov) for 11 Aug Tropical Squall, 17 Aug High-Shear Tropical, and 23 Feb Tropical Convection; P. Marinescu (peter.marinescu@colostate.edu) for ACPC Scattered CLN, ACPC Scattered POL, and MC3E Squall; J. Bukowski (jenbukow@ucla.edu) for Isolated Tropical WRF and Supercell WRF; and L. Grant (leah.grant@colostate.edu) for Isolated Tropical 250m, Isolated Tropical 500m, Multicells CTL, Multicells H50, Multicells M25, Supercell CTL, Supercell H50, Supercell M25, and Tropical Squall.

REFERENCES

Barth, M. C., and Coauthors, 2015: The Deep Convective Clouds and Chemistry (DC3) field campaign. *Bull. Amer. Meteor. Soc.*, **96**, 1281–1309, https://doi.org/10.1175/BAMS-D-13-00290.1.

Bergeron, T., 1935: On the physics of clouds and precipitation. *Proc. Fifth Assembly*, Lisbon, Portugal, International Union of Geodesy and Geophysics, 156–180.

Betts, A. K., 1976: The thermodynamic transformation of the tropical subcloud layer by precipitation and downdrafts. *J. Atmos. Sci.*, **33**, 1008–1020, https://doi.org/10.1175/1520-0469(1976)033<1008:TTTOTT>2.0.CO;2.

Browning, K. A., and G. B. Foote, 1976: Airflow and hail growth in supercell storms and some implications for hail suppression. *Quart. J. Roy. Meteor. Soc.*, **102**, 499–533, https://doi.org/10.1002/qj.49710243303.

Bryan, G. H., J. C. Wyngaard, and J. M. Fritsch, 2003: Resolution requirements for the simulation of deep moist convection. *Mon. Wea. Rev.*, **131**, 2394–2416, https://doi.org/10.1175/1520-0493(2003)131<2394:RRFTSO>2.0.CO;2.

Cotton, W. R., G. D. Alexander, R. Hertenstein, R. L. Walko, R. L. McAnelly, and M. Nicholls, 1995: Cloud venting—A review and some new global annual estimates. *Earth-Sci. Rev.*, **39**, 169–206, https://doi.org/10.1016/0012-8252(95)00007-0.

——, G. H. Bryan, and S. C. van den Heever, 2010: *Storm and Cloud Dynamics*. 2nd ed. Academic Press, 820 pp.

Dauhut, T., J.-P. Chaboureau, J. Escobar, and P. Mascart, 2015: Large-eddy simulations of Hector the Convector making the stratosphere wetter. *Atmos. Sci. Lett.*, **16**, 135–140, https://doi.org/10.1002/asl2.534.

Dennis, E. J., and M. R. Kumjian, 2017: The impact of vertical wind shear on hail growth in simulated supercells. *J. Atmos. Sci.*, **74**, 641–663, https://doi.org/10.1175/JAS-D-16-0066.1.

Doswell, C. A., H. E. Brooks, and R. A. Maddox, 1996: Flash flood forecasting: An ingredients-based methodology. *Wea. Forecasting*, **11**, 560–581, https://doi.org/10.1175/1520-0434(1996)011<0560:FFFAIB>2.0.CO;2.

Feingold, G., and A. J. Heymsfield, 1992: Parameterizations of condensational growth of droplets for use in general circulation models. *J. Atmos. Sci.*, **49**, 2325–2342, https://doi.org/10.1175/1520-0469(1992)049<2325:POCGOD>2.0.CO;2.

Fierro, A. O., J. Simpson, M. A. LeMone, J. M. Straka, and B. F. Smull, 2009: On how hot towers fuel the Hadley cell: An observational and modeling study of line-organized convection in the equatorial trough from TOGA COARE. *J. Atmos. Sci.*, **66**, 2730–2746, https://doi.org/10.1175/2009JAS3017.1.

——, E. J. Zipser, M. A. LeMone, J. M. Straka, and J. M. Simpson, 2012: Tropical oceanic hot towers: Need they be undilute to transport energy from the boundary layer to the upper troposphere effectively? An answer based on trajectory analysis of a simulation of a TOGA COARE convective system. *J. Atmos. Sci.*, **69**, 195–213, https://doi.org/10.1175/JAS-D-11-0147.1.

Findeisen, W., 1938: Kolloid-meteorologische Vorgänge bei Neiderschlags-bildung. *Meteor. Z.*, **55**, 121–133.

Grant, L. D., and S. C. van den Heever, 2014: Microphysical and dynamical characteristics of low-precipitation and classic supercells. *J. Atmos. Sci.*, **71**, 2604–2624, https://doi.org/10.1175/JAS-D-13-0261.1.

——, and ——, 2015: Cold pool and precipitation responses to aerosol loading: Modulation by dry layers. *J. Atmos. Sci.*, **72**, 1398–1408, https://doi.org/10.1175/JAS-D-14-0260.1.

——, ——, Z. S. Haddad, J. Bukowski, P. J. Marinescu, R. L. Storer, D. J. Posselt, and G. L. Stephens, 2021: Namelists Associated with "A Linear Relationship Between Vertical Velocity and Condensation Processes in Deep Convection." Colorado State University Libraries, https://doi.org/10.25675/10217/233963.

Haddad, Z. S., O. O. Sy, S. Hristova-Veleva, and G. L. Stephens, 2017: Derived observations from frequently sampled microwave measurements of precipitation—Part I: Relations to atmospheric thermodynamics. *IEEE Trans. Geosci. Remote Sens.*, **55**, 3441–3453, https://doi.org/10.1109/TGRS.2017.2671598.

Heikenfeld, M., B. White, L. Labbouz, and P. Stier, 2019: Aerosol effects on deep convection: The propagation of aerosol perturbations through convective cloud microphysics. *Atmos. Chem. Phys.*, **19**, 2601–2627, https://doi.org/10.5194/acp-19-2601-2019.

Jensen, E. J., S. C. van den Heever, and L. D. Grant, 2018: The life cycles of ice crystals detrained from the tops of deep convection. *J. Geophys. Res. Atmos.*, **123**, 9624–9634, https://doi.org/10.1029/2018JD028832.

Korolev, A. V., and I. P. Mazin, 2003: Supersaturation of water vapor in clouds. *J. Atmos. Sci.*, **60**, 2957–2974, https://doi.org/10.1175/1520-0469(2003)060<2957:SOWVIC>2.0.CO;2.

Kumjian, M. R., and K. Lombardo, 2020: A hail growth trajectory model for exploring the environmental controls on hail size: Model physics and idealized tests. *J. Atmos. Sci.*, **77**, 2765–2791, https://doi.org/10.1175/JAS-D-20-0016.1.

Lebo, Z. J., and H. Morrison, 2015: Effects of horizontal and vertical grid spacing on mixing in simulated squall lines and implications for convective strength and structure. *Mon. Wea. Rev.*, **143**, 4355–4375, https://doi.org/10.1175/MWR-D-15-0154.1.

Luo, Z. J., G. Y. Liu, and G. L. Stephens, 2010: Use of A-Train data to estimate convective buoyancy and entrainment rate. *Geophys. Res. Lett.*, **37**, L09804, https://doi.org/10.1029/2010GL042904.

Marinescu, P. J., S. C. van den Heever, S. M. Saleeby, and S. M. Kreidenweis, 2016: The microphysical contributions to and

evolution of latent heating profiles in two MC3E MCSs. *J. Geophys. Res. Atmos.*, **121**, 7913–7935, https://doi.org/10.1002/2016JD024762.

——, ——, ——, ——, and P. J. DeMott, 2017: The microphysical roles of lower-tropospheric versus midtropospheric aerosol particles in mature-stage MCS precipitation. *J. Atmos. Sci.*, **74**, 3657–3678, https://doi.org/10.1175/JAS-D-16-0361.1.

——, and Coauthors, 2021: Impacts of varying concentrations of cloud condensation nuclei on deep convective cloud updrafts—A multimodel assessment. *J. Atmos. Sci.*, **78**, 1147–1172, https://doi.org/10.1175/JAS-D-20-0200.1.

McGee, C. J., and S. C. van den Heever, 2014: Latent heating and mixing due to entrainment in tropical deep convection. *J. Atmos. Sci.*, **71**, 816–832, https://doi.org/10.1175/JAS-D-13-0140.1.

Mechem, D. B., R. A. Houze Jr., and S. S. Chen, 2002: Layer inflow into precipitating convection over the western tropical Pacific. *Quart. J. Roy. Meteor. Soc.*, **128**, 1997–2030, https://doi.org/10.1256/003590002320603502.

Morrison, H., J. A. Curry, and V. I. Khvorostyanov, 2005: A new double-moment microphysics parameterization for application in cloud and climate models. Part I: Description. *J. Atmos. Sci.*, **62**, 1665–1677, https://doi.org/10.1175/JAS3446.1.

——, G. Thompson, and V. Tatarskii, 2009: Impact of cloud microphysics on the development of trailing stratiform precipitation in a simulated squall line: Comparison of one- and two-moment schemes. *Mon. Wea. Rev.*, **137**, 991–1007, https://doi.org/10.1175/2008MWR2556.1.

Nelson, S. P., 1983: The influence of storm flow structure on hail growth. *J. Atmos. Sci.*, **40**, 1965–1983, https://doi.org/10.1175/1520-0469(1983)040<1965:TIOSFS>2.0.CO;2.

Nielsen, E. R., and R. S. Schumacher, 2018: Dynamical insights into extreme short-term precipitation associated with supercells and mesovortices. *J. Atmos. Sci.*, **75**, 2983–3009, https://doi.org/10.1175/JAS-D-17-0385.1.

Paluch, I. R., and C. A. Knight, 1984: Mixing and the evolution of cloud droplet size spectra in a vigorous continental cumulus. *J. Atmos. Sci.*, **41**, 1801–1815, https://doi.org/10.1175/1520-0469(1984)041<1801:MATEOC>2.0.CO;2.

Pan, L. L., and Coauthors, 2014: Thunderstorms enhance tropospheric ozone by wrapping and shedding stratospheric air. *Geophys. Res. Lett.*, **41**, 7785–7790, https://doi.org/10.1002/2014GL061921.

Park, J. M., S. C. Heever, A. L. Igel, L. D. Grant, J. S. Johnson, S. M. Saleeby, S. D. Miller, and J. S. Reid, 2020: Environmental controls on tropical sea breeze convection and resulting aerosol redistribution. *J. Geophys. Res. Atmos.*, **125**, e2019JD031699, https://doi.org/10.1029/2019JD031699.

Pinsky, M., I. P. Mazin, A. Korolev, and A. Khain, 2013: Supersaturation and diffusional droplet growth in liquid clouds. *J. Atmos. Sci.*, **70**, 2778–2793, https://doi.org/10.1175/JAS-D-12-077.1.

Politovich, M. K., and W. A. Cooper, 1988: Variability of the supersaturation in cumulus clouds. *J. Atmos. Sci.*, **45**, 1651–1664, https://doi.org/10.1175/1520-0469(1988)045<1651:VOTSIC>2.0.CO;2.

Posselt, D. J., S. van den Heever, G. Stephens, and M. R. Igel, 2012: Changes in the interaction between tropical convection, radiation, and the large-scale circulation in a warming environment. *J. Climate*, **25**, 557–571, https://doi.org/10.1175/2011JCLI4167.1.

Reutter, P., and Coauthors, 2009: Aerosol- and updraft-limited regimes of cloud droplet formation: Influence of particle

number, size and hygroscopicity on the activation of cloud condensation nuclei (CCN). *Atmos. Chem. Phys.*, **9**, 7067–7080, https://doi.org/10.5194/acp-9-7067-2009.

Riehl, H., and J. S. Malkus, 1958: On the heat balance in the equatorial trough zone. *Geophysica*, **6**, 503–538.

Rogers, R. R., and M. K. Yau, 1989: *A Short Course in Cloud Physics*. 3rd ed. Elsevier, 304 pp.

Schiro, K. A., F. Ahmed, S. E. Giangrande, and J. D. Neelin, 2018: GoAmazon2014/5 campaign points to deep-inflow approach to deep convection across scales. *Proc. Natl. Acad. Sci. USA*, **115**, 4577–4582, https://doi.org/10.1073/pnas.1719842115.

Skamarock, W. C., and Coauthors, 2019: A description of the Advanced Research WRF Model version 4. NCAR Tech. Note NCAR/TN-556+STR, 145 pp., https://doi.org/10.5065/1dfh-6p97.

Squires, P., 1952: The growth of cloud drops by condensation. I. General characteristics. *Aust. J. Chem.*, **5**, 59–86, https://doi.org/10.1071/CH9520059.

Stephens, G. L., and Coauthors, 2020: A distributed small satellite approach for measuring convective transports in the Earth's atmosphere. *IEEE Trans. Geosci. Remote Sens.*, **58**, 4–13, https://doi.org/10.1109/TGRS.2019.2918090.

Storer, R. L., and D. J. Posselt, 2019: Environmental impacts on the flux of mass through deep convection. *Quart. J. Roy. Meteor. Soc.*, **145**, 3832–3845, https://doi.org/10.1002/qj.3669.

Sy, O. O., Z. S. Haddad, G. L. Stephens, and S. Hristova-Veleva, 2017: Derived observations from frequently sampled microwave measurements of precipitation. Part II: Sensitivity to atmospheric variables and instrument parameters. *IEEE Trans. Geosci. Remote Sens.*, **55**, 2898–2912, https://doi.org/10.1109/TGRS.2017.2656061.

van den Heever, S. C., L. D. Grant, G. L. Stephens, Z. S. Haddad, R. L. Storer, O. O. Sy, and D. J. Posselt, 2018: The challenges of representing vertical motion in numerical models. *Proc. SPIE*, **10782**, 1078204, https://doi.org/10.1117/12.2501584.

Wang, L., and J. Chen, 2019: Efficient determination of cloud drop number concentration near the cloud base with parameterization based on fundamental theory and parcel model simulations. *J. Geophys. Res. Atmos.*, **124**, 6467–6483, https://doi.org/10.1029/2018JD029648.

Wegener, A., 1911: *Thermodynamik der Atmosphäre*. J. A. Barth, 331 pp.

Zipser, E. J., 1977: Mesoscale and convective-scale downdrafts as distinct components of squall-line structure. *Mon. Wea. Rev.*, **105**, 1568–1589, https://doi.org/10.1175/1520-0493(1977)105<1568:MACDAD>2.0.CO;2.

——, 2003: Some views on "hot towers" after 50 years of tropical field programs and two years of TRMM data. *Cloud Systems, Hurricanes, and the Tropical Rainfall Measuring Mission (TRMM), Meteor. Monogr.*, No. 51, Amer. Meteor. Soc., 49–58.